Materials Research. 2018; 21(3): e20171044
DOI: http://dx.doi.org/10.1590/1980-5373-MR-2017-1044

Microstructural Characterization of a Laser Surface Remelted Cu-Based Shape Memory Alloy

Murillo Romero da Silva[a]*, Piter Gargarella[b], Witor Wolf[a], Tobias Gustmann[c], Claudio Shyinti Kiminami[b], Simon Pauly[c], Jürgen Eckert[d,e], Claudemiro Bolfarini[b]

[a]Universidade Federal de São Carlos, Programa de Pós-Graduação em Ciência e Engenharia de Materiais, Rodovia Washington Luís, km 235, 13565-905, São Carlos, SP, Brasil
[b]Departamento de Engenharia de Materiais, Universidade Federal de São Carlos, Rodovia Washington Luís, km 235, 13565-905, São Carlos, SP, Brasil
[c]Institut für komplexe Materialien, Leibniz-Institut fur Festkorper- und Werkstoffforschung Dresden, Helmholtzstra ße, 20, D-01069, Dresden, Sachsen, Deutschland
[d]Erich Schmid Institute of Materials Science, Austrian Academy of Sciences, Jahnstraße,12, A-8700, Leoben, Steiermark, Österreich
[e]Department Materialphysik, Montanuniversität Leoben, Jahnstraße,12, A-8700, Leoben, Österreich

Received: November 27, 2017; Accepted: March 02, 2018

Cu-based shape memory alloys (SMAs) present some advantages as higher transformation temperatures, lower costs and are easier to process than traditional Ti-based SMAs but they also show some disadvantages as low ductility and higher tendency for intergranular cracking. Several studies have sought for a way to improve the mechanical properties of these alloys and microstructural refinement has been frequently used. It can be obtained by laser remelting treatments. The aim of the present work was to investigate the influence of the laser surface remelting on the microstructure of a Cu-11.85Al-3.2Ni-3Mn (wt%) SMA. Plates were remelted using three different laser scanning speeds, i.e. 100, 300 and 500 mm/s. The remelted regions showed a T-shape morphology with a mean thickness of 52, 29 and 23 μm and an average grain size of 30, 29 and 23μm for plates remelted using scanning speed of 100, 300 and 500 mm/s, respectively. In the plates remelted with 100 and 300 mm/s some pores were found at the root of the keyhole due to the keyhole instability. We find that the instability of keyholes becomes more pronounced for lower scanning speeds. It was not observed any preferential orientation introduced by the laser treatment.

Keywords: *microstructure, rapid solidification, laser.*

1. Introduction

Shape memory alloys (SMAs) are a class of smart materials that exhibit a property known as shape memory effect (SME)[1,2]. The SME can be defined as the ability to recover the original shape and size of a specimen after plastic deformation by heating the alloy above a critical temperature[1,2]. This effect is related to a thermoelastic martensitic transformation and a crystallographic subgroup relation between austenitic and martensitic phases[1].

SMAs have attracted significant attention and interest in recent years for a wide range of commercial applications, due to the outstanding properties that they present. Among the prominent commercial applications, the biomedical industry stands out as the most well-established area in the production of SMAs, mostly in the form of stents, guide wires and arthroscopic instruments[3-5]. In addition, the application of SMAs in the electronic industry is in good progress as well due to the growing interest in the use of shape memory based actuators[3,6].

Among the most common SMAs, Cu-Al-Ni SMAs have been developed as a cheap and competitive alternative to the traditional and expensive Ti-based SMA[7,8]. In fact, Cu-Al-Ni SMAs show some advantageous properties compared with Ti-based SMAs, like an excellent behavior on micro and nano scale, which provides a competitive advantage to the function in sensors and actuators in micro electro-mechanical systems[9]. Furthermore, Cu-based SMAs when compared with Ti-based SMAs present relatively low cost of raw materials and processing, better thermal and electrical conductivity, easiness to process and higher transformation temperatures[7,8,10,11].

However, Cu-Al-Ni SMAs present worse mechanical properties than Ti-based SMAs, showing low ductility, low fatigue life and tendency for intergranular cracking[1,7]. For this reason, some applications are limited and an improvement in the mechanical properties is required in order to make these SMAs suitable for application in industry. The ductility has been considerably improved by the addition of Mn to Cu-Al-Ni SMAs without resulting in a significant change of

*e-mail: murilloromero_@hotmail.com

the transformation temperatures[1,7,11]. The addition of other alloying elements such as Zr, as well as thermomechanical treatments, powder metallurgy and rapid solidification have been used to further improve the ductility of Cu-based SMAs[2,12-15].

Another important feature of Cu-Al-Ni SMAs is the necessity of rapid cooling during processing of the alloy, in order to ensure the formation of the metastable martensitic phase β'_1, which is the responsible for the SME[9,13]. Slow equilibrium cooling causes the precipitation of stable phases, which would inhibit the martensitic transformation and therefore the SME[9]. Processes with a high cooling rate can be usually employed not only to ensure the β'_1 phase formation but also to efficiently reduce the grain size and therefore improve the mechanical properties[13,16-19]. An economical and efficient way to apply high cooling rates of up to 10^{10} K/s is laser surface remelting[20]. It results in a local microstructural refinement that affects not only the mechanical behavior but also the thermal stability of the alloy[10] and may also induce a level of anisotropy[10,13,21,22].

In our previous work[10], we have studied the effect of laser surface remelting on the mechanical properties and thermal behavior of a Cu-11.85Al-3.2Ni-3Mn (wt%) SMA. We found that this treatment is an effective method to improve the mechanical properties without considerable changes in the thermal stability. In the present work, a systematic microstructural characterization is carried out in order to further investigate the effect of laser surface remelting on the phase formation and microstructure in order to better correlate the above mentioned findings with the applied processing.

2. Materials and Methods

The experimental procedure used to obtain the remelted plates was described in details in da Silva et al.[10]. The samples were named according to the scanning speed applied: 100 (PLT_100), 300 (PLT_300) and 500 mm/s (PLT_500). The as-cast sample (non-remelted sample) will be referred as PLT_untreated. The remelted samples were produced using a laser beam power of 300 W and a track overlap of 50 %.

The microstructural characterization was carried out using optical (OM), scanning (SEM) and transmission electron microscopy (TEM), employing a Nikon EPIPHOT-300 optical microscope, a Hitachi Tabletop Microscope TM-1000 SEM and a Philips CM-120 transmission electron microscope, respectively. OM and SEM samples were prepared by grinding up to a 1500 grit sand paper, polishing using a 1 μm colloidal silica solution and etching with a solution of H_2O:HNO_3 (2:1). The grain size of the samples was measured using the method described by Sutou et al.[23].

TEM samples were prepared by grinding the samples down to a thickness of 80 μm using sand paper and subsequently thinned by argon ion milling. X-ray diffraction (XRD) experiments were performed using a STOE STADI P diffractometer with Mo-$K\alpha_1$ ($\lambda = 0,7093$ Å) radiation source. About 100 μm thick samples were analyzed in transmission mode. To achieve this thickness, the samples were manually ground using sandpaper with gris of 120 and 600.

For electron backscatter diffraction (EBSD) and energy-dispersive X-ray spectroscopy (EDS) analysis a SEM FEI Inspect S 50 equipped with an EDAX-AMETEK™ EBSD detector was used. In the EDS analysis a vertical and a horizontal EDS line was drawn on the remelted layer of the plates, in order to observe if there was selective element vaporization during the laser treatment. In addition, EDS element mapping was performed on the samples. EBSD analyses were used to investigate the grain and twin orientation in the remelted layer and the volume fraction of phases in the plates. For the EBSD analyses we used a structural file of the martensitic monoclinic β'_1 phase (space group P21/m). The EBSD analyses were conducted with a step size scan between 0.3 and 0.6 μm. Points with a confidence index (CI) of less than 0.1 were not taken into account.

3. Results and Discussion

The microstructure was first investigated by OM and SEM. Figures 1(a) and (b) display images for the PLT_untreated sample, showing only the presence of monoclinic martensite β'_1 phase (a = 0.443 nm, b = 0.530 nm, c = 1.278 nm and $\beta = 95.8°$, with space group P21/m[10,18]), which exhibits a zig-zag morphology, which is in accordance with the literature[1,11,13,24,25]. The grains show a columnar morphology due to the plate solidification process by suction casting. The mean grain size is 123 ± 13 μm and the mean porosity measured by the Archimedes principle is only 1.4 ± 0.7%. The cooling rate during the suction casting was estimated to be 8.5 x 10^3 K/s[10].

Figures 2(a), (b) and (c) show OM and SEM images of the PLT_100 samples. The remelted layer exhibits a T-shape morphology. This T-shape is due the Gaussian distribution of the laser beam energy with maximum power around the center associated with the small laser beam spot size of 80 μm applied during the laser treatment[21]. The region remelted in the center of the laser incident, i.e., the T vertical component, is known as keyhole[26,27]. The keyhole consists in a slender vapor cavity present in the interaction region between the laser beam and the substrate[26,28]. The mean keyhole length found for the PLT_100 samples is 506 ± 117 μm. The thickness of the remelted surface layers is about 52 ± 14 μm. In the two regions of the T, remelted layer and keyhole, there is a refinement of the grains yielding a mean grain size of 30 ± 8 μm in this area. The grain refinement can be better seen in SEM images (Figure 2(c)) of the cross section of the remelted coating where several single tracks overlap each other.

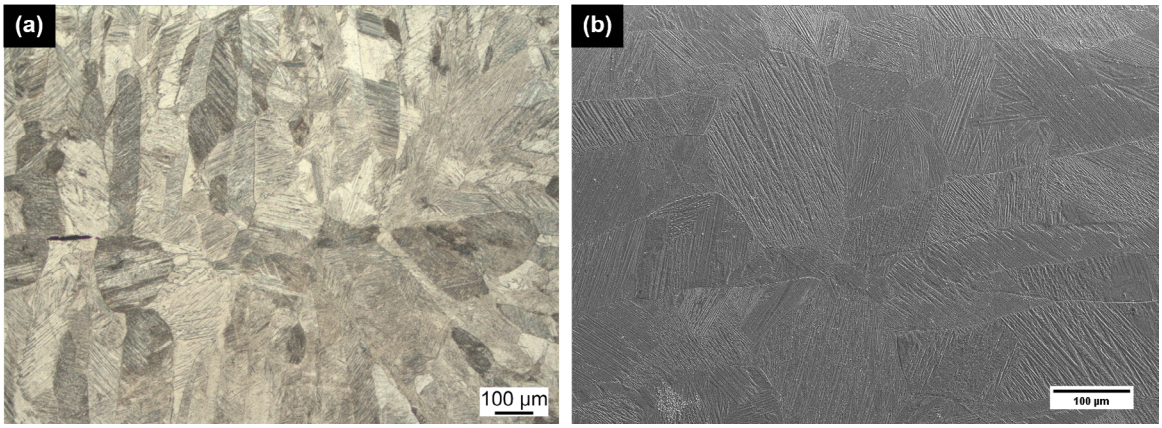

Figure 1. (a) OM and **(b)** SEM - secondary electron images of a PLT_untreated sample. Elongated β'_1 martensite grains with zig-zag morphology can be seen.

At the end of the keyhole we found large pores with a diameter varying from 50 to 200 µm (Figure 2(a)). These pores are formed due the instability of the keyhole during the process, when there is a break on the capillarity causing bubble formation at the keyhole root[28]. Since there is an eddy flux, forward and downward, around the keyhole interface, the bubbles cannot escape from the molten pool, remaining entrapped, and thus causing porosity at the end of the laser treatment. The formed bubbles are due to the vaporization during the process, which can be general or selective[29]. EDS analysis was conducted on the remelted region in order to observe if a selective vaporization of some alloying element during the process, which can affect some thermal properties of the alloy. This analysis will be discussed later.

It is expected that a heat affect zone (HAZ) with a course microstructure forms around the remelted region, as usually observed in laser processing[21,30]. This region is difficult to identify in our case (as shown in Figure 2) because the base material presents a similar microstructure as observed around the remelted region.

Figure 2(d) corresponds to a PLT_300 sample, revealing the same T-shape morphology as found for PLT_100 samples. However, the mean keyhole length is lower (241 ± 103) and the mean remelted layer is thinner (29 ± 5 µm). The same behavior of the remelted coating is observed for PLT_500 samples, with a mean keyhole length of 159 ± 16 µm and a mean remelted layer of 22 ± 3 µm. These values are again smaller than for PLT_300 samples. The remelted coating (cross section) of the PLT_500 samples is displayed in Figure 2(e). The mean grain size in the remelted layer is 29 ± 5 µm for the PLT_300 and 23 ± 3 µm for the PLT_500 samples.

These differences observed among the three laser treated samples are due to the different scanning speeds used in the process. A higher scanning speed provides a lower laser interaction time with the surface of the samples, and thus, a lower fraction of material is remelted culminating with lower keyhole length and remelted layer thickness. Furthermore, high scanning speed leads to a higher cooling rate, promoting more pronounced grain refinement. The cooling rate of the PLT_100, PLT_300 and PLT_500 samples was estimated as 8.25 x 10^5, 2.48 x 10^6 and 4.13 x 10^6 K/s, respectively[10]. When compared with the suction casting process, the laser treated samples show smaller grains, since the cooling rate of the laser process is two orders of magnitude higher than that of suction casting.

The presence of pores at end of the keyhole is also observed for the PLT_300 samples but it is much less pronounced compared to the PLT_100 samples. These pores have a diameter varying from 60 to 80 µm. It is believed that the reason for pore formation is the same as discussed for the PLT_100 samples. The PLT_500 samples do not show any pore formation after the laser treatment. The quantity of remelted material is related with the pore formation during the process; for PLT_300 and PLT_500 samples the fraction of remelted material does not seem to be able to cause the instability of the keyhole and, hence porosity formation is less pronounced in these samples.

Another result from the shorter interaction time provided through a higher scanning speed is the reduced number of coarse grains in the HAZ for the PLT_500 samples. The interaction time is very short, and the laser heat input seems to be not high enough to cause coarsening of the grains adjacent to the melt pool.

Only the martensitic β'_1 phase was observed after the laser treatment in all samples. Its zig-zag morphology can be easily seen on the SEM images (Figures 2(c) and (e)). A more sophisticated analysis was carried out using EBSD (see bellow) in order to guarantee that the martensitic β'_1 phase is the only one present on the laser treated samples.

EDS analyses were performed in order to obtain the chemical composition of the investigated samples. For the PLT_untreated material, the composition was analyzed by comparing a minimum of eight measurement points. The mean values of the chemical composition of the untreated sample are listed in Table 1.

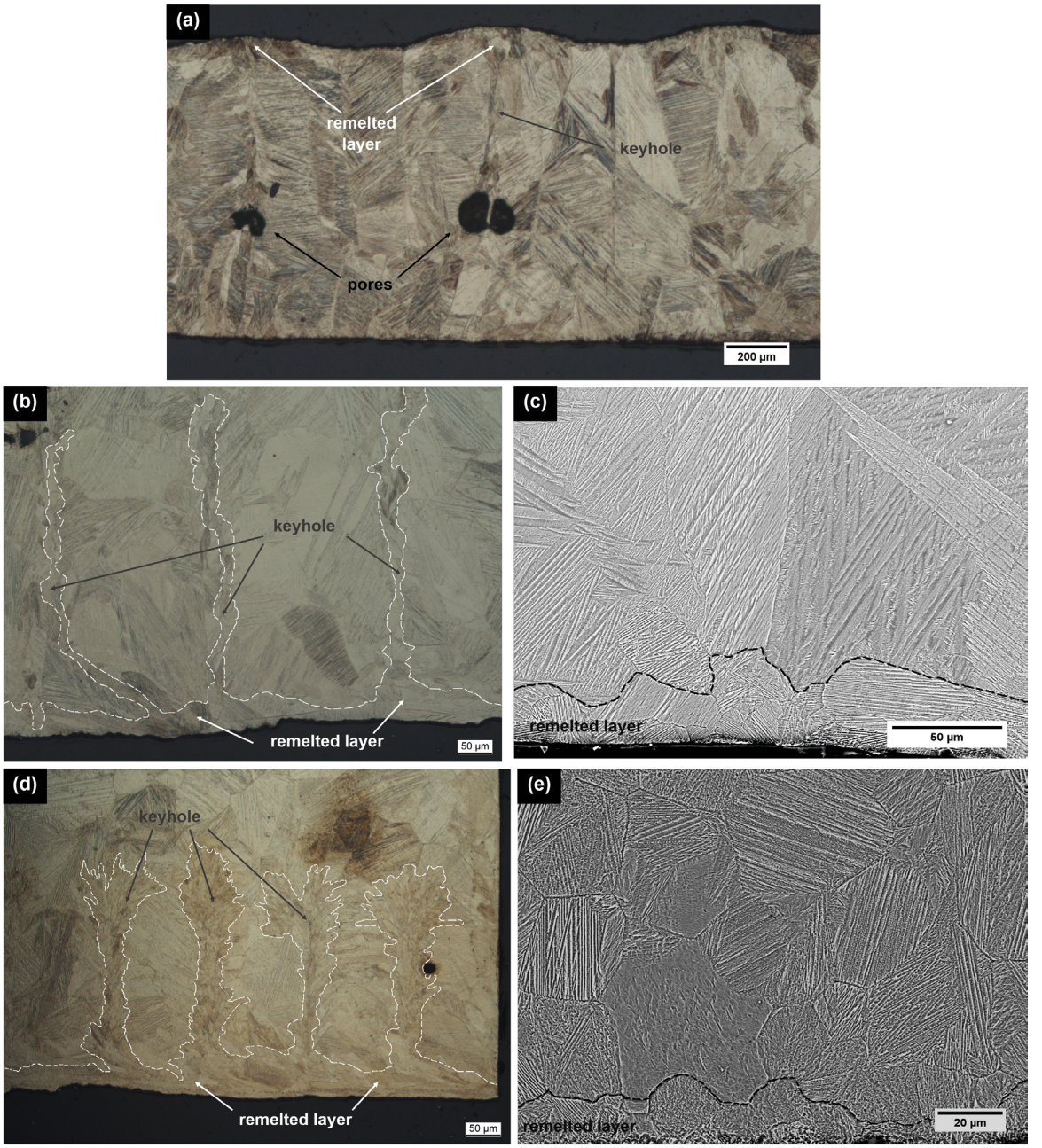

Figure 2. (a) and **(b)** OM image of single tracks (cross section) and **(c)** SEM - secondary electron mage of the remelted coating (cross section) of a PLT_100 sample; **(d)** OM image of single tracks (cross section) of a PLT_300 sample and **(e)** SEM image of the remelted coating (cross section) of a PLT_500 sample. The remelted region can be observed, which has a T-shape morphology and fine grains. In addition, pores are present at the root of the remelted region of the PLT_100 sample.

Table 1. Chemical composition of the PLT_untreated material according to EDS analysis

	Cu (wt%)	Al (wt%)	Ni (wt%)	Mn (wt%)	TOTAL (wt%)
EDS values	80.9 ± 0.2	13.0 ± 0.2	3.1 ± 0.1	3.1 ± 0.1	100
Nominal	82	11.8	3.2	3	100

Comparing the mean values obtained by EDS with the theoretical nominal composition (reference) revels a good agreement for Ni and Mn. However, the values for Cu and Al differ by 1.1 and 1.2 wt%, respectively. This difference is small and can be attributed to processing, which may cause small compositional modifications through physical and chemical reactions, or due to the low accuracy of equipment used for the analyses. Despite this composition difference, the alloy composition of the samples is within a reasonable range for this work, i.e., it is still in the composition range that allows the formation of the desired microstructure responsible for SME, in good agreement with the OM and SEM images.

As already stated above, chemical analyses by EDS line scanning of the laser treated samples were performed in order to investigate if general or selective vaporization occurred. The EDS lines were allocated in the T-shape remelted region, using a horizontal and a vertical line for each track investigated. Alloying element mapping on the remelted single tracks was also performed to complement the analyses. Figures 3 and 4 show the EDS line scanning and EDS mapping results, respectively, for the PLT_100 samples.

The results of the EDS line analyses are very similar for the three different types of samples, in both vertical and horizontal scanning directions. There are no composition changes along the lines, and the measured composition values are close to the nominal composition (Figure 3). The absence of a composition change along the EDS lines shows that the vaporization is general and negligible in the laser surface remelting process. Thus, there is no selectivity in the process, as would be expected for Al, which has a lower vaporization temperature than Cu, Ni, and Mn. The laser input energy is sufficiently large, thus providing generalized vaporization, which culminates with the destabilization of the keyhole and porosity formation at the base of the keyhole.

The EDS maps are similar for the three different types of samples. All alloying elements are homogeneously distributed in the laser treated samples (Figure 4). These results confirm the absence of selective vaporization during laser processing, and reveal that the vaporization is of general nature.

A more detailed analysis of phase formation and grain orientation after laser treatment was carried out by EBSD. The results are show in Figures 5 and 6.

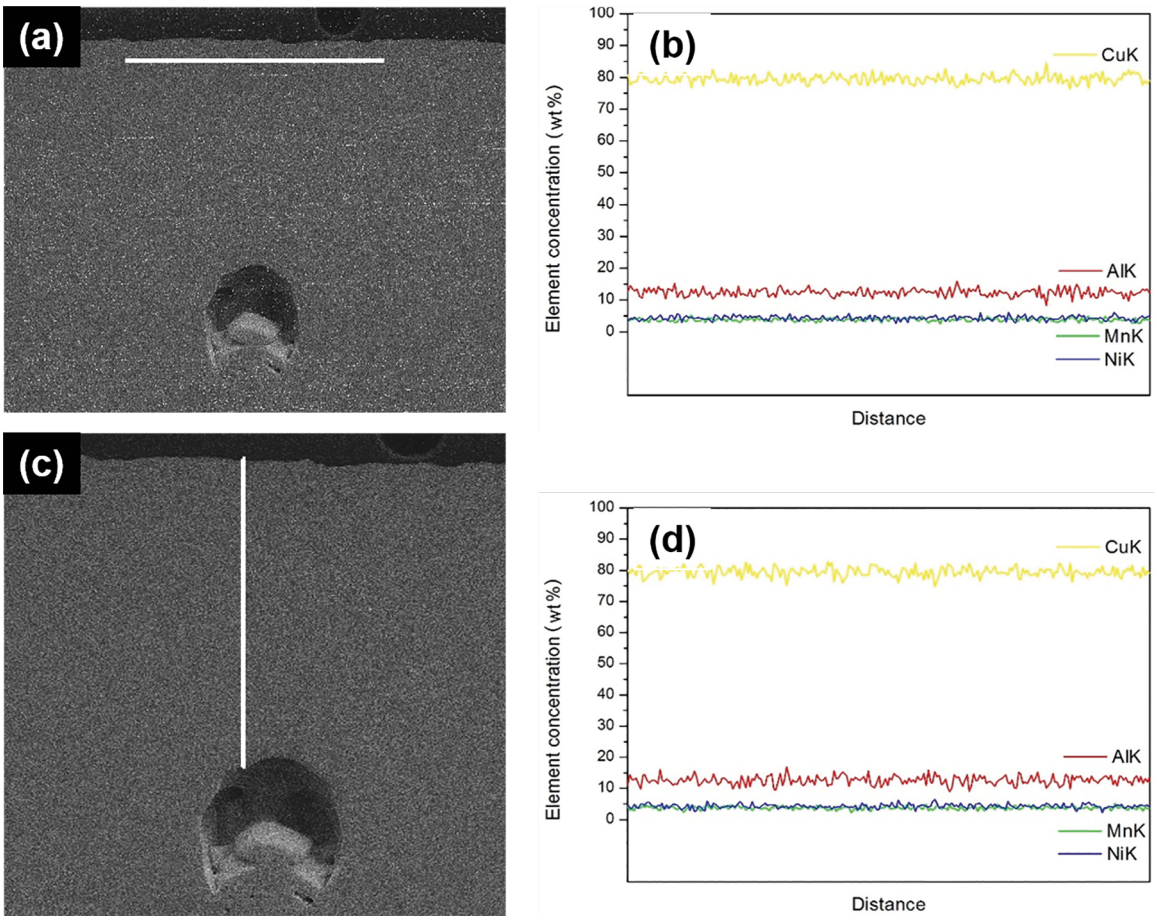

Figure 3. EDS line of the remelted region of PLT_100. **(a)** Micrography along a horizontal line and **(b)** their respective graphic: line distance x element concentration (wt%) **(c)** Micrography along a vertical line and **(d)** their respective graphic: line distance x element concentration (wt%). For the horizontal line the distance increases from left to right, and for the vertical line from up to down.

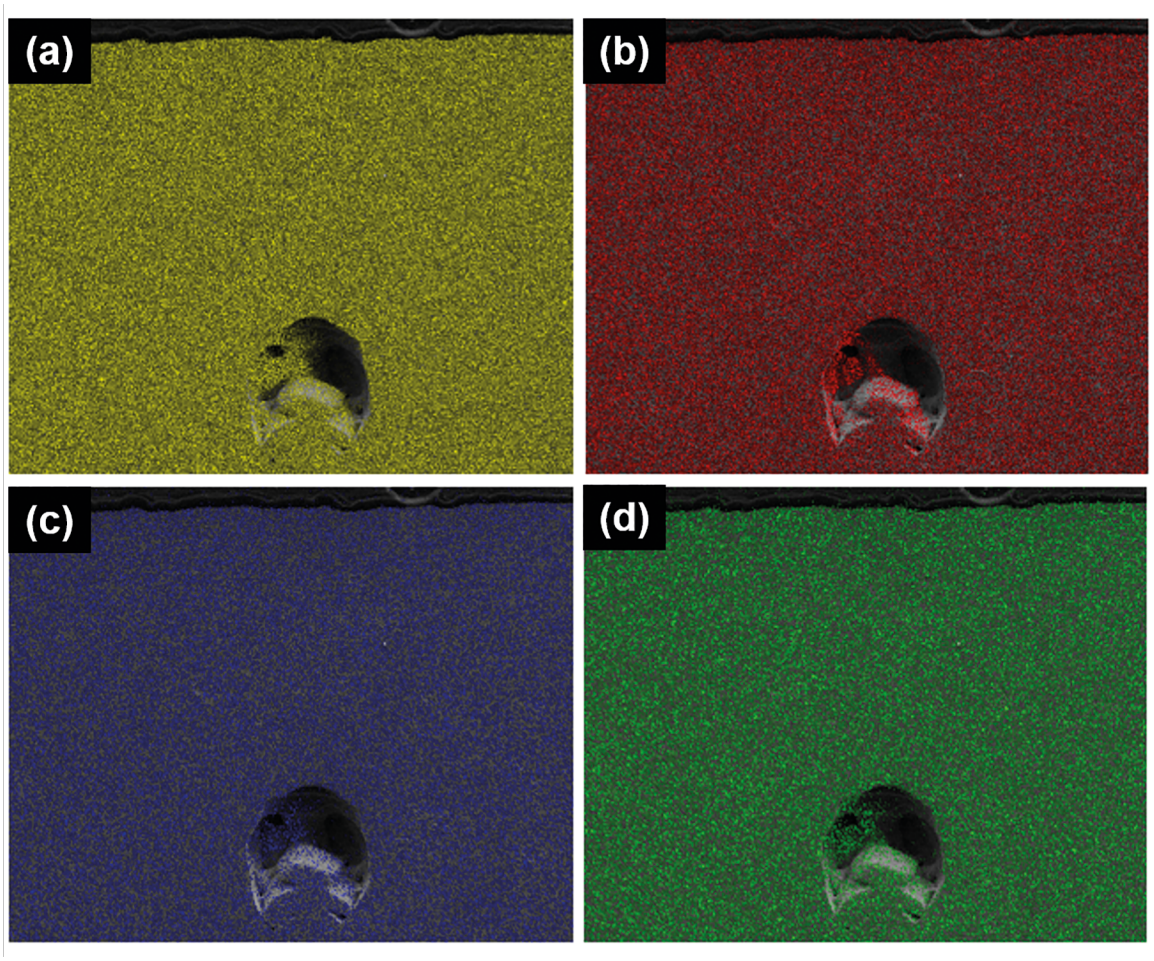

Figure 4. EDS maps of a PLT_100 sample at the remelted region: **(a)** Cu, **(b)** Al, **(c)** Ni e **(d)** Mn.

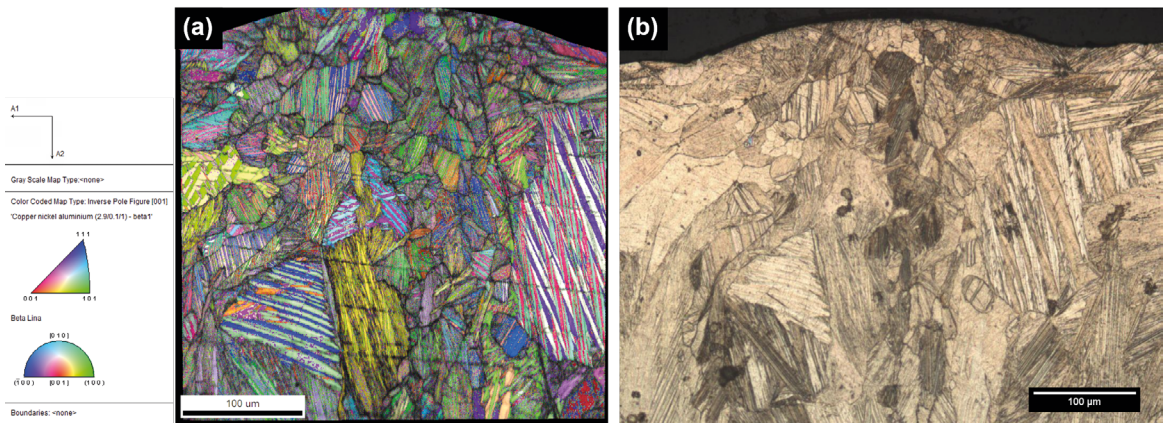

Figure 5. EBSD/OIM maps and data for a single track of a PLT_100 sample. **(a)** Inverse pole figure (IPF) overlapped with the image quality map (IQ) showing the preferential orientation of twin planes and grains and **(b)** respective OM image.

Figure 5(a) reveals that the grains in the PLT_100 samples have no preferential orientation after the laser surface treatment. The observed grains and twin orientations are random. A higher magnification inverse pole figure (IPF) mapping at the same track observed in Figure 5(a) allow a better analysis of the refined grains in the remelted region (Figure S1). As discussed for Figure 5(a), the grains in the remelted track as well as in HAZ/base material are randomly oriented. However, there is a preferential orientation of the twin planes, which exhibit an angle of approximately ± 30º

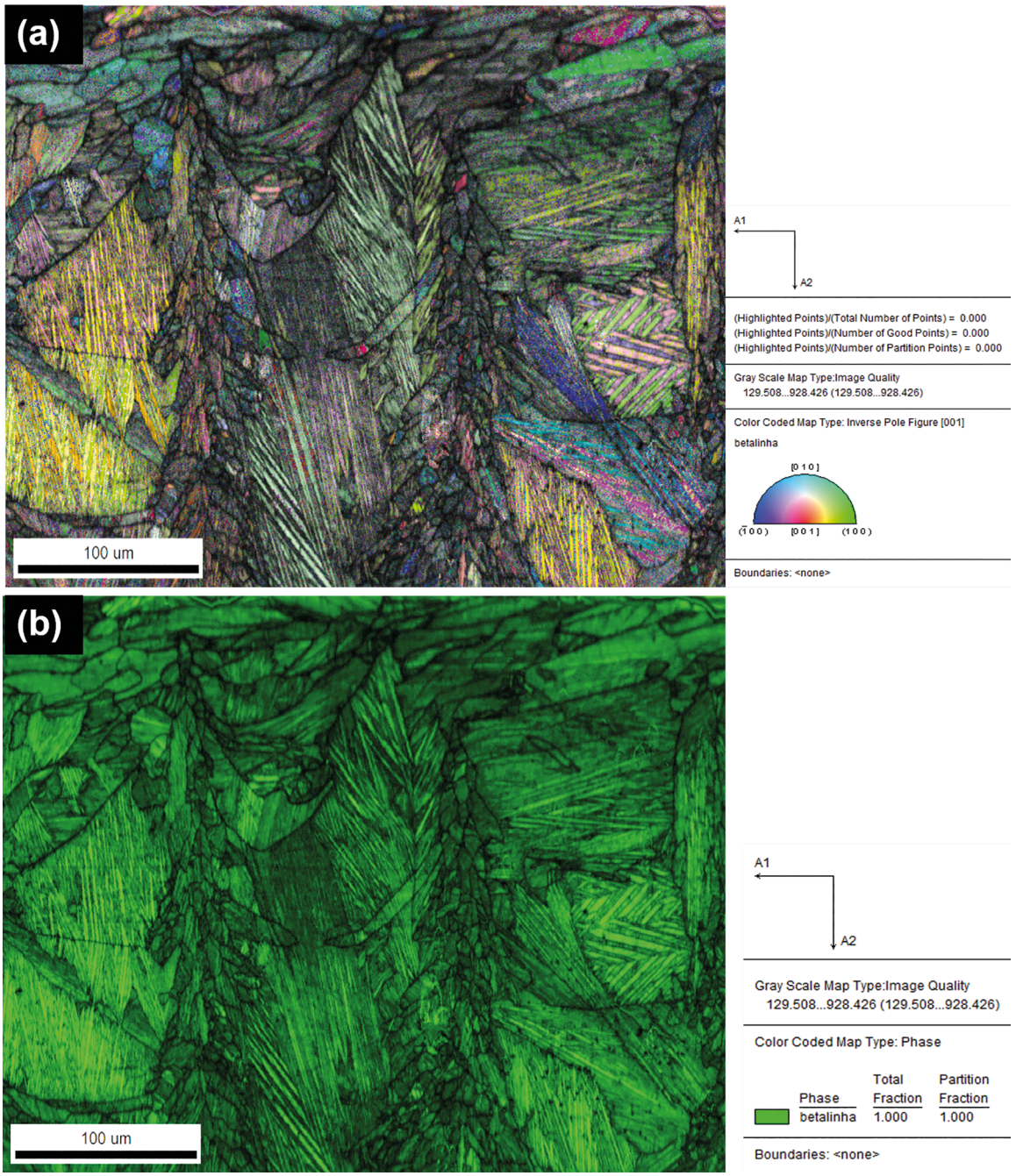

Figure 6. EBSD/OIM maps and data for the single tracks of a PLT_300 sample. **(a)** Inverse pole figure (IPF) overlapped with the image quality map (IQ) showing the random orientation of the grains and twin planes, and **(b)** overlapped image phase map with image quality image (IQ) showing the absence of black dots inside the grains, indicating that the monoclinic β'_1 phase is the only one present in the sample.

relative to the vertical line of the keyholes in the remelted region. The heat extraction direction during cooling assists preferential orientation of the twin, which are established adjacent to the remelted track. These preferentially oriented twins may improve the tensile mechanical properties due to anisotropy in the material. An EBSD/OIM (orientation imaging microscopy) data map obtained from the remelted layer of a PLT_300 sample (Figure 6) gives no hint for preferentially grown grains or twin planes with preferential orientation but they are rather arranged randomly (Figure 6(a)). These findings indicate that the laser surface remelting treatment does not produce any preferential orientation in the remelted region or in the HAZ/base material. A preferential twin plane orientation was observed only in one sample, which suggests that this is an atypical behavior.

Figure 6(b) shows a phase map obtained using only the structural file of the martensitic β'_1 phase (Figure 6(b)). We checked the image quality (IQ) with the overlapping map of phases, where the black dots generated correspond to points where the backscattered electron diffraction patterns of the sample showed low confidence index values, i.e., the black spots do not match any phase inserted in the map data. These regions with black dots correspond to grain boundaries, twin boundaries or defects. The dots in green in Figure 6(b) correspond to the monoclinic β'_1 phase, as can be concluded from the good confidence indexes for all scanning directions. Only the β'_1 phase was observed throughout the sample, with the black dots (low values of the confidence index) allocated on grain boundaries. These findings corroborate the OM and SEM results and reveal that no new phases form during the laser surface remelting treatment, but only the martensitic monoclinic β'_1 phase is present in the investigated samples.

The laser treated samples were also investigated by transmission electronic microscopy (TEM). Characteristic images are shown in Figure 7. Again, the martensitic monoclinic β'_1 phase is the only phase that can be indexed in all samples analyzed. Hence, also the TEM results are in agreement with the OM, SEM and EBSD analyses. Figure 7(a) show the electron diffraction pattern of the monoclinic β'_1 phase indexed for the PLT_100 sample.

Figures 7(b) and (c) display the typical lamellar structure of the monoclinic β'_1 phase. The assembly of the lamellae forms twinned martensite laths with zig-zag morphology. The lamellae are refined in all analyzed samples, presenting a mean thickness of 255 ± 58 nm. The grain size is directly proportional to the thickness of the lamellae. Hence, the

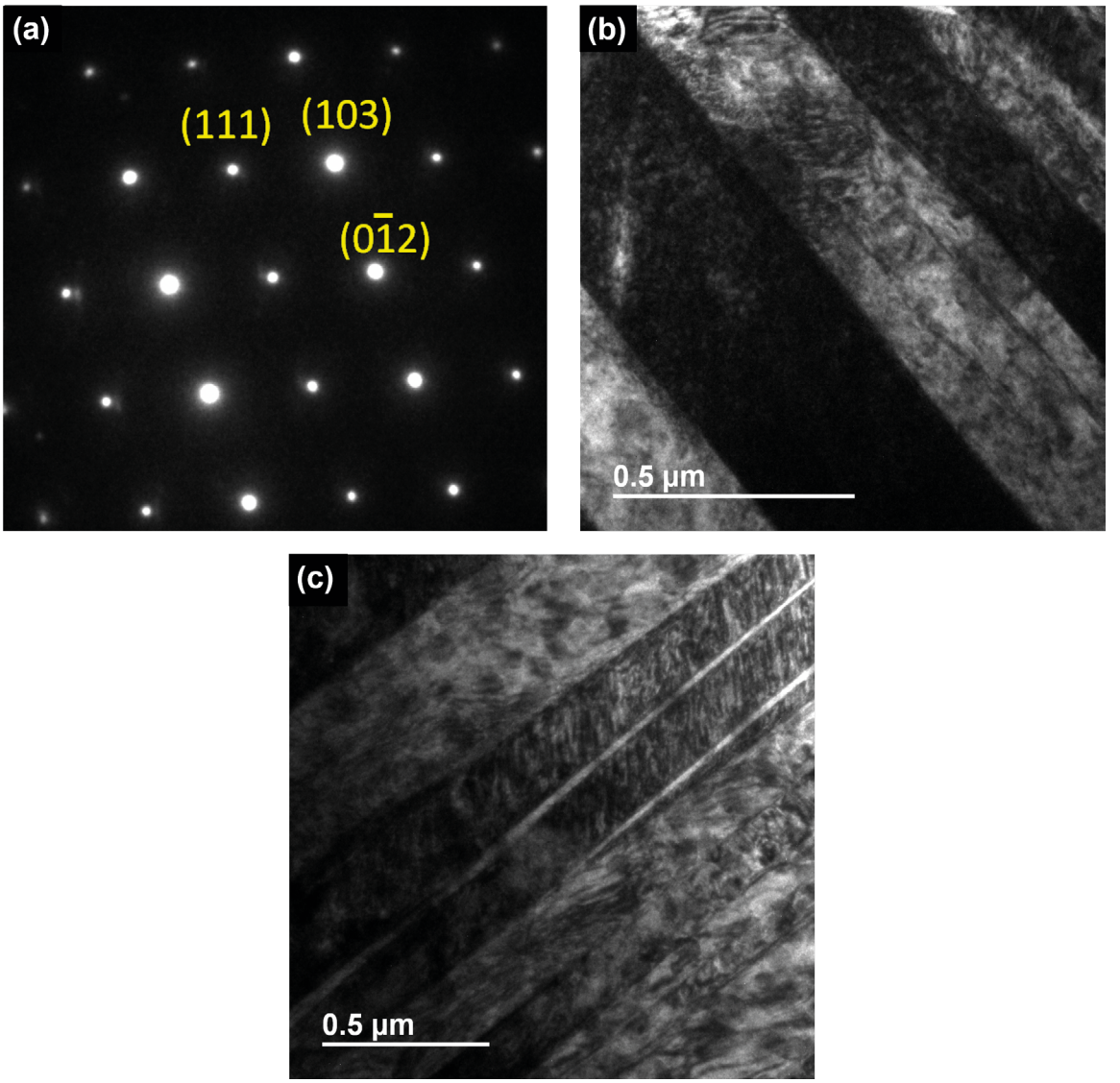

Figure 7. (a) Electron diffraction pattern of the [-3 1 2] zone axis of the monoclinic β'_1 phase and **(b)** and **(c)** TEM bright field images of PLT_100 and PLT_300 samples, showing twinned martensite laths.

refinement of the lamellae is similar as the observed grain refinement.

The phase formation in the samples was also investigated by XRD and the results are depicted in Figure 8. The XRD results prove that only the martensitic β'_1 monoclinic phase was formed. The differences observed in peak intensities may be due the different grain sizes and amout of defects.

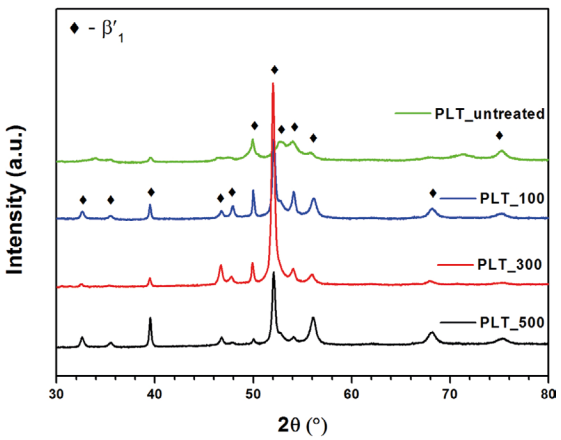

Figure 8. XRD diffraction patterns for the as-cast and laser treated samples. The four samples present the same peaks, which correspond to the monoclinic β'_1 martensitic phase.

4. Conclusions

The influence of laser surface remelting on the microstructure of Cu-11.85Al-3.2Ni-3Mn (wt%) SMA plates was investigated. The following conclusions can be drawn:

1. Laser surface treatment does not produce new phases in the SMA alloy investigated. Only the martensitic β'_1 monoclinic phase was observed irrespective of the applied remelting parameters.
2. The grains in the remelted region are significantly refined if compared with the as-cast material and the non-remelted areas. Grain sizes of 30 ± 8, 29 ± 5 and 23 ± 3 µm were obtained for PLT_100, PLT_300 and PLT_500 samples, respectively.
3. A larger grain refinement is obtained for samples remelted with higher scanning speed. This is attributed to the lower interaction time of the laser beam, which provides a higher cooling rate during fast processing when compared with the lowest scanning speeds employed.
4. Keyhole formation due to general vaporization occurs during the laser treatment. Pores form at the root of the remelted areas, and their formation is related with the keyhole instability, which is correlated with the scanning speed of the laser. The volume fraction of pores forming at the root of the keyhole tends to decrease with increasing scanning speed.
5. The laser treatment does not generate a preferential orientation of the twin planes or grains in the remelted region nor in the HAZ/base material. All samples show a random orientation after the laser remelting treatment.

5. Acknowledgements

The authors are thankful to Michael Frey and Vitor Anibal Mendes for technical assistance and helpful discussions. Financial support granted by FAPESP (São Paulo Research Foundation) (2015/04134-7 and 2013/05987-8), CNPq (National Council of Technological and Scientific Development) (132132/2015-0) and CAPES (Brazil's Federal Agency for the Support and Improvement of Higher Education) (024/12) under the program BRAGECRIM (BEX 7185/13-8) in collaboration with DFG (German Research Foundation) (EC 111/28-1).

6. References

1. Otsuka K, Wayman CME, eds. *Shape Memory Materials*. Cambridge: Cambridge University Press; 1998.
2. Zhu JH. *The effect of rapid solidification on martensitic transformation in a copper-based shape memory alloy*. [Dissertation]. Wollongong: University of Wollongong, Department of Materials Engineering; 1994.
3. Jani JM, Leary M, Subic A, Gibson MA. A review of shape memory alloy research, applications and opportunities. *Materials & Design (1980-2015)*. 2014;56:1078-1113.
4. Petrini L, Migliavacca F. Biomedical Applications of Shape Memory Alloys. *Journal of Metallurgy*. 2011;2011:501483.
5. Michael A, Pequegnat A, Wang J, Zhou YN, Khan MI. Corrosion performance of medical grade NiTi after laser processing. *Surface and Coatings Technology*. 2017;324:478-485.
6. Van Humbeeck J. Non-medical applications of shape memory alloys. *Materials Science and Engineering: A*. 1999;273-275:134-148.
7. Lojen G, Gojić M, Anže I. Continuously cast Cu-Al-Ni shape memory alloy - Properties in as-cast condition. *Journal of Alloys and Compounds*. 2013;580:497-505.
8. Sutou Y, Omori T, Wang JJ, Kainuma R, Ishida K. Characteristics of Cu-Al-Mn-based shape memory alloys and their applications. *Materials Science and Engineering: A*. 2004;378(1-2):278-282.
9. López-Ferreño I, Breczewski T, López GA, Nó ML, San Juan J. Stress-assisted atomic diffusion in metastable austenite D03 phase of Cu-Al-Be shape memory alloys. *Scripta Materialia*. 2016;124:155-159.
10. da Silva MR, Gargarella P, Gustmann T, Botta Filho WJ, Kiminami CS, Eckert J, et al. Laser surface remelting of a Cu-Al-Ni-Mn shape memory alloy. *Materials Science and Engineering: A*. 2016;661:61-67.
11. Mazzer EM, Kiminami CS, Bolfarini C, Cava RD, Botta WJ, Gargarella P. Thermodynamic analysis of the effect of annealing

on the thermal stability of a Cu-Al-Ni-Mn shape memory alloy. *Thermochimica Acta*. 2015;608:1-6.

12. Dutkiewicz J, Czeppe T, Morgiel J. Effect of titanium on structure and martensic transformation in rapidly solidified Cu-Al-Ni-Mn-Ti alloys. *Materials Science and Engineering: A*. 1999;273-275:703-707.

13. Cava RD, Bolfarini C, Kiminami CS, Mazzer EM, Botta Filho WJ, Gargarella P, et al. Spray forming of Cu-11.8Al-3.2Ni-3Mn (wt%) shape memory alloy. *Journal of Alloys and Compounds*. 2013;615:S602-S606.

14. de Damborenea J. Surface modification of metals by high power lasers. *Surface and Coatings Technology*. 1998;100-101:377-382.

15. Gustmann T, dos Santos JM, Gargarella P, Kühn U, Van Humbeeck J, Pauly S. Properties of Cu-Based Shape-Memory Alloys Prepared by Selective Laser Melting. *Shape Memory and Superelasticity*. 2017;3(1):24-36.

16. Gustmann T, Neves A, Kühn U, Gargarella P, Kiminami CS, Bolfarini C, et al. Influence of processing parameters on the fabrication of a Cu-Al-Ni-Mn shape-memory alloy by selective laser melting. *Additive Manufacturing*. 2016;11:23-31.

17. Mazzer EM, Kiminami CS, Gargarella P, Cava RD, Basilio LA, Bolfarini C, et al. Atomization and Selective Laser Melting of a Cu-Al-Ni-Mn Shape Memory Alloy. *Materials Science Forum*. 2014;802:343-348.

18. Gargarella P, Kiminami CS, Mazzer EM, Cava RD, Basilio LA, Bolfarini C, et al. Phase Formation, Thermal Stability and Mechanical Properties of a Cu-Al-Ni-Mn Shape Memory Alloy Prepared by Selective Laser Melting. *Materials Research*. 2015;18(Suppl 2):35-38.

19. Oliveira JP, Zeng Z, Omori T, Zhou N, Miranda RM, Braz Fernandes FM. Improvement of damping properties in laser processed superelastic Cu-Al-Mn shape memory alloys. *Materials & Design*. 2016;98:280-284.

20. Massalski TB, Woychik CG. Modelling of the nucleation temperature of the f.c.c. phase competing with glass formation in Cu-Ti alloys. *Acta Metallurgica*. 1985;33(10):1873-1886.

21. Ready JF, ed. *LIA Handbook of Laser Materials Processing.* Berlin Heidelberg New York: Springer-Verlag; 2001. p. 223-280.

22. Thijs L, Kempen K, Kruth JP, Van Humbeeck J. Fine-structured aluminium products with controllable texture by selective laser melting of pre-alloyed AlSi10Mg Powder. *Acta Materialia*. 2013;61(5):1809-1819.

23. Sutou Y, Omori T, Kainuma R, Ishida K. Grain size dependence of pseudoelasticity in polycrystalline Cu-Al-Mn-based shape memory sheets. *Acta Materialia*. 2013;61(10):3842-3850.

24. Otsuka K, Ohba T, Tokonami M, Wayman CM. New description of long period stacking order structures of martensites in ß-phase alloys. *Scripta Metallurgica et Materialia*. 1993;29(10):1359-1364.

25. Mazzer EM, Gargarella P, Cava C, Bolfarini C, Galano M, Kiminami CS. Effect of dislocations and residual stresses on the martensitic transformation of Cu-Al-Ni-Mn shape memory alloy powders. *Journal of Alloys and Compounds*. 2017;723:841-849.

26. Pang S, Chen X, Zhou J, Shao X, Wang C. 3D transient multiphase model for keyhole, vapour plume, and weld pool dynamics in laser welding including the ambient pressure effect. *Optics and Lasers in Engineering*. 2015;74:47-58.

27. Chen M, Xu J, Xin L, Zhao Z, Wu F, Ma S, et al. Effect of keyhole characteristics on porosity formation during pulsed laser-GTA hybrid welding of AZ31B magnesium alloy. *Optics and Lasers in Engineering*. 2017;93:139-145.

28. Berger P, Hügel H, Graf T. Understanding Pore Formation in Laser Beam Welding. *Physics Procedia*. 2011;12(Pt A):241-247.

29. Harooni M, Carlson B, Strohmeier BR, Kovacevic R. Pore formation mechanism and its mitigation in laser welding of AZ31B magnesium alloy in lap joint configuration. *Materials & Design*. 2014;58:265-276.

30. He B, Cheng X, Li J, Tian XJ, Wang HM. Effect of laser surface remelting and low temperature aging treatments on microstructures and surface properties of Ti-55511 alloy. *Surface and Coatings Technology*. 2017;316:104-112.

Supplementary Material

The following online material is available for this article:

Figure S1. EBSD/OIM maps and data for the single track of PLT_100 sample showing the inverse pole figure (IPF) overlapped with the image quality map (IQ). The twin plans and grains present a random orientation.